Traveling ionospheric disturbances propagating ahead of the Tohoku-Oki tsunami: a case study,

E. A. Kherani, L. Rolland, Ph. Lognonne, A. Sladen, V. Klausner, E.R. de Paula

Geophysical Journal International

Geophys. J. Int. (2016) **204,** 1148–1158 doi: 10.1093/gji/ggv500
GJI Gravity, geodesy and tides

Traveling ionospheric disturbances propagating ahead of the Tohoku-Oki tsunami: a case study

E.A. Kherani,[1] L. Rolland,[2] P. Lognonné,[3] A. Sladen,[2] V. Klausner[4] and E.R. de Paula[1]

[1]*Instituto Nacional de Pesquisas Espaciais (INPE), SP* 12227010*, Brazil. E-mail: esfhan.kherani@inpe.br*
[2]*GeoAzur, Nice, F*-06560*, France*
[3]*Institut de Physique du Globe de Paris (IPGP) Paris, F*-75005*, France*
[4]*University of Vale do Paraiba (UNIVAP), SP* 12244000*, Brazil*

Accepted 2015 November 16. Received 2015 November 11; in original form 2015 February 26

SUMMARY

We document two kinds of traveling ionospheric disturbances, namely, CTIDs (Co-tsunami-Traveling-Ionospheric-disturbances) and ATIDs (Ahead-of-Tsunami-Traveling-Ionospheric-disturbances) related to the Tohoku-Oki tsunami of 2011 March 11. They are referred to the disturbances that remain behind and ahead of the principal tsunami wave front, respectively. We first note their presence in a numerical experiment performed using a simulation code coupling the tsunami, atmosphere and ionosphere. This code uses the tsunami wavefield as an input and simulates acoustic-gravity waves (AGWs) in the atmosphere and TIDs, in the form of total electron content (TEC) disturbance, in the ionosphere. The simulated TEC reveals the excitation of CTIDs (at about 2 TECU) and ATIDs (at about 1 TECU), representing up to 5 per cent disturbance over the ambient electron density, and they arise from the dissipation of AGWs in the thermosphere. A novel outcome is that during the tsunami passage between ∼6° and 12° of epicentral distance, strong ATIDs arrive ∼20–60 min ahead of the tsunami wave front covering ∼3°–10° of distance from the tsunami location. Simulation results are compared with the far-field observations using GNSS satellites and confirm that ATIDs are the first detected TEC maximum, occurring 20–60 min ahead of the tsunami arrival. Our simulation also confirms the presence of largest TEC maximum representing CTIDs, 10–20 min after the first tsunami wave. ATIDs reported in this study have characteristics that can be potentially used for the early warning of the tsunami.

Key words: Acoustic-gravity waves; Ionosphere/atmosphere interactions; Tsunamis; Early warning.

1 INTRODUCTION

A magnitude $M_w = 9.0$ Tohoku-Oki earthquake occurred at 05:46:23 UT off the northeast coast of Japan (USGS epicentre located at 38.322°N, 142.369°E). Waves generated in the solid earth, ocean, atmosphere and ionosphere were detected by acceleration, displacement and pressure sensors on the Earth surface and ocean bottom, (e.g. Maeda *et al.* 2011; Simons *et al.* 2011; Bletery *et al.* 2014), by various ionospheric sensors such as GPS dual frequency sensors and all-sky imagers monitoring the anomalies in the ionosphere (Heki 2011; Makela *et al.* 2011; Astafyeva *et al.* 2013) and by identifying the atmospheric disturbances using GOCE accelerometer (Garcia *et al.* 2014).

For this tsunami, number of studies report detailed features of the total electron content (TEC) disturbances or Co-Tsunami-TIDs (CTIDs) excited behind the principal tsunami wave front (Astafyeva *et al.* 2011; Chen *et al.* 2011; Liu *et al.* 2011; Rolland *et al.* 2011; Tsugawa *et al.* 2011; Galvan *et al.* 2012). These features include the excitation of near-field elongated elliptical and far-field circular wave fronts that propagate with a wide range of phase velocities covering the velocities of the acoustic to gravity waves (GWs). Based on Tsunami–Atmosphere–Ionosphere (TAI) coupling through dissipative acoustic-gravity waves (AGWs), numerical simulations of these CTIDs are also presented (Matsumura *et al.* 2011; Kherani *et al.* 2012). This mechanism was first proposed by Heki & Ping (2005) to explain the observed horizontally spreading of the CTIDs during an earthquake. Unlike previous simulation studies that were confined to either pure acoustic or GWs, these numerical studies had considered complete dissipative AGWs dynamics, that led to the excitation of secondary AGWs in the thermosphere. Moreover, using the realistic tsunami wavefield as an input, simulation presented by Kherani *et al.* (2012) could capture varieties of wave fronts, propagating with acoustic wave speed ∼600 m s^{-1}, GW speed ∼250 m s^{-1} and slow speed <200 m s^{-1}

associated with the tsunami that were observed in the form of CTIDs. The study also explained the development of CTIDs within 6 min from the tsunami initiation, as reported by Astafveya *et al.* (2011).

In their study, Kherani *et al.* (2012) focused on CTIDs though it also revealed the presence of another kind of TIDs which we now refer to as ATIDs (Earlier-arriving-than-tsunami-Traveling-Ionospheric-disturbances). The present work aims to investigate dynamics of these ATIDs based on simulation and observations. In the simulation, we examine two scenarios: a dominant secondary GWs scenario and a complete secondary AGWs scenario. These two comparative scenarios are chosen to investigate diverse effects of secondary GWs/AGWs to excite different kinds of TIDs. In particular, we explore possibility that the realistic AGWs scenario can generate ATIDs ahead of the tsunami since their horizontal propagation in the upper thermosphere is faster than the tsunami in the ocean. We also search for such ATIDs in the GNSS observations of TIDs at several far-field locations.

2 TSUNAMI-ATMOSPHERE-IONOSPHERE (TAI) COUPLED SIMULATION MODEL

The TAI coupled simulation model is described in detail by Kherani *et al.* (2012). It is based on TAI coupling mechanism which is accomplished in three steps: (i) excitation of tsunami wavefield by the coseismic rupture, (ii) subsequent excitation of AGWs by the tsunami wavefield and (iii) subsequent excitation of ionospheric disturbances by AGWs. The tsunami wavefield modeling is performed following the method described by Hébert *et al.* (2001) and Sladen *et al.* (2010), by using the preliminary source of USGS for Tohoku-Oki tsunami (provided at http://earthquake.usgs.gov/earthquakes). Simulation of tsunami-induced AGWs in the atmosphere is performed using the following hydrodynamic Navier–Stokes equations (Kherani *et al.* 2011, 2012).

$$\frac{\partial^2 \vec{W}'}{\partial t^2} = \frac{\gamma p}{\rho}\nabla^2 \vec{W}' + (\nabla.\vec{W})\frac{1}{\rho}\nabla(\gamma p) - \frac{\nabla p}{\rho^2}\nabla.(\rho \vec{W}') + \frac{1}{\rho}\nabla(\vec{W}'.\nabla)p + \frac{\partial}{\partial t}\left(\nu\nabla^2 \vec{W}' + (\zeta' + \frac{\nu}{3})\nabla(\nabla.\vec{W}')\right) - \frac{\partial}{\partial t}(\vec{W}'.\nabla \vec{W}') \quad (1)$$

$$\vec{W}' = \vec{W} + \vec{W}_b$$

$$\frac{\partial \rho}{\partial t} + \nabla.(\rho \vec{W}') = 0; \quad (2)$$

$$\frac{\partial p}{\partial t} + (\vec{W}'.\nabla)p + \gamma p \nabla.\vec{W}' = 0 \quad (3)$$

where $\vec{W}$ is the perturbation wind (or the amplitude of AGWs), W_b is the background wind derived from the Horizontal Wind model, ($p = R\rho T$, ρ, T) are the atmospheric pressure, mass density and temperature, (μ, ζ) are the dynamic first and second viscosities, ($\nu = \mu/\rho$, $\zeta' = \zeta/\rho$) are the first and second kinematic viscosities and (γ) is the adiabatic exponent.

Simulation of TIDs in the ionosphere is performed using the following set of hydromagnetic equations (Kherani *et al.* 2009, 2012):

$$\frac{\partial \vec{u}_s}{\partial t} = \frac{q_s}{m_s}(\vec{E} + \vec{u}_s \times \vec{B}) - \nu_s \vec{u}_s + \nu_s \vec{W}, \quad (4)$$

$$\frac{\partial n_s}{\partial t} + \nabla.(n_s \vec{u}_s) = P - L, \quad (5)$$

$$\nabla^2 \vec{E} - \nabla(\nabla.\vec{E}) - \frac{1}{c^2}\frac{\partial^2 \vec{E}}{\partial t^2} - \mu_o \frac{\partial \vec{J}}{\partial t} = 0, \quad (6)$$

$$\vec{J} = \underline{\sigma}.\vec{E} + \vec{J}_w; \quad \vec{J}_w = e(n_i \vec{u}_i^w - n_e \vec{u}_e^w), \quad (7)$$

$$\nabla^2 \vec{B} - \frac{1}{c^2}\frac{\partial^2 \vec{B}}{\partial t^2} = -\mu_o \nabla \times \vec{J}. \quad (8)$$

Here (n_s, $\vec{u}_s$) are the number density, velocity of plasma fluid 's' ($s = i$ for ions/e for electrons), ($q_i = +Z_i e$, $q_e = -e$, $Z_i = 1$), ($\vec{E}$, $\vec{B}$, $\vec{J}$) are the electric field, magnetic field and net current, ($\vec{W}$) is the amplitude of AGWs derived from eq. (1), ($\vec{u}_i^w$, $\vec{u}_e^w$) in eq. (7) are the ion and electron velocities without the electric field as derived from eq. (4) and $\vec{J}_w$ is the corresponding current density. $\vec{B}_o$ is the Earth's magnetic field, ν_s is the frequency of collision between species s-to neutral, $\underline{\sigma}$ is the ionospheric conductivity tensor and ($c = \frac{1}{\sqrt{\mu_o \epsilon_o}}$) is the speed of light in vacuum. P, L are the production and loss of ions and electrons by photo ionization and chemical reactions. The production term 'P' in (5) is derived from SAMI2 model (Huba *et al.* 2000). The chemical loss term, 'L', in (5) is retained through effective recombination rate as taken by Kherani *et al.* (2011). In addition to the wave eq. (6), $\vec{E}$ also satisfies the charge neutrality condition given by the following equation (Kherani *et al.* 2012):

$$\nabla.\vec{J} = 0 \quad \text{or} \quad \nabla.(\sigma.\vec{E} + \vec{J}_w) = 0 \Rightarrow \nabla.\vec{E} = -\sigma^{-1}(\vec{E}.\nabla\sigma + \nabla.J_w). \quad (9)$$

Eqs (1)–(9) form a closed set of equations to study the temporal and spatial variations of AGWs wind $\vec{W}$, atmospheric density/pressure (ρ, p), ionospheric number density (n), electric field $\vec{E}$ and magnetic field $\vec{B}$ disturbances. At $t = 0$ corresponding to the origin time (5:46:23 UT) of the tsunami, the ambient atmosphere and ionosphere (p_o, ρ_o, n_o, ν, T) are obtained from the SAMI2 model (Huba *et al.* 2000). In Fig. 1, from (a) to (d), the atmospheric mass density (ρ_o), acoustic speed $\left(c_s = \sqrt{\gamma p/\rho}\right)$, zonal/meridional wind components of the background wind ($\vec{W}_b$) and the ionospheric number density (n_o) are shown. Ambient altitude profiles shown in this figure correspond to fixed latitude and longitude of the epicentre though in the present simulation, these parameters also vary with latitude and longitude. The ambient electric field is considered to be zero.

Eqs (1)–(9) are solved numerically using a finite-difference method in a three dimension spherical simulation domain that consists of altitude, latitude and longitude. The implicit Crank–Nicholson scheme is employed to perform the time integration leading to a matrix equation that is subsequently solved by the Successive-Over-Relaxation method. The magnetic dipole coordinate system (p, q, ϕ) is adopted where p, q, ϕ represent the coordinates outward normal to the Earth's magnetic field, northward directed parallel to the Earth's magnetic field and azimuth angle (positive towards west), respectively. The N-S and E-W boundaries

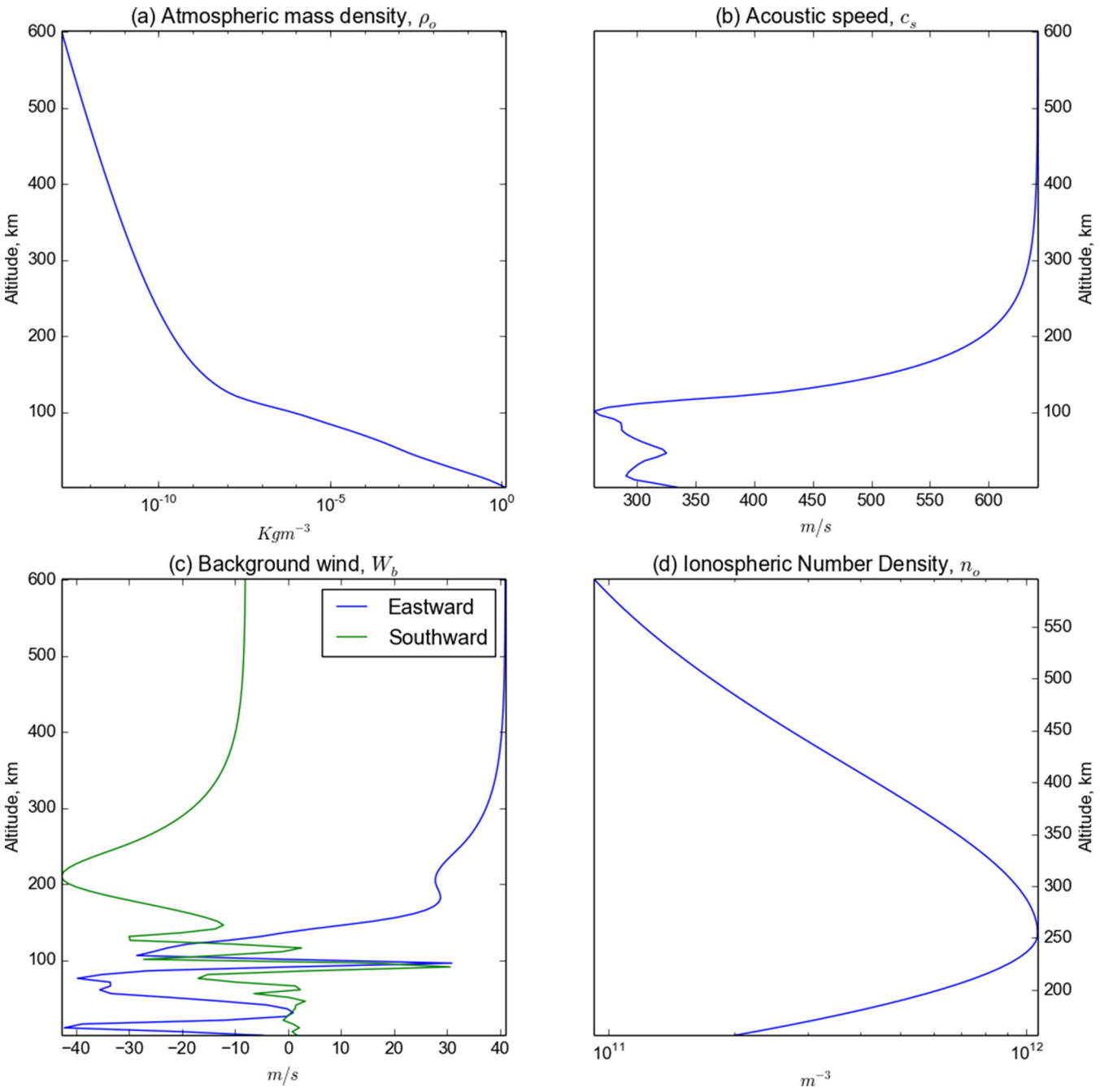

Figure 1. Ambient atmosphere and ionosphere parameters as a function of altitude above the epicentre: (a) atmospheric mass density, (b) atmospheric acoustic speed, (c) atmospheric mean wind and (d) ionospheric number density. (ρ_o, n_o) represent the densities at time $t = 0$ which is beginning time (5:46 UT) of the tsunami.

of simulation domain are 13°S–70°N and 120–186°E which covers the region of interest. The upper boundary is chosen to be 600 km for both the atmosphere and ionosphere. The lower boundary for the atmosphere and ionosphere are chosen to be the ocean surface and 160 km, respectively. The E region of ionosphere that lies below 160 km altitude couples with the overlying F region through the geomagnetic field lines and AGWs dissipated in the E region can disturb the F region through this electrodynamic coupling. Note however that this study does not include E region and subsequent coupling dynamics.

At the lower boundary, that is, at the ocean–atmosphere interface, the outward normal component W_p of the wind $\vec{W}$ is continuous and equals to W_T for all time where W_T is the tsunami wavefield obtained from the tsunami simulation model (Sladen *et al.* 2010). The lower boundary condition $W_p = W_T$ at all time acts as the driving source for the excitation of AGWs. At the subsequent time, other wind components W_q, W_ϕ in entire simulation domain and W_p in entire simulation domain except at the lower boundary are self-consistently determined from the eq. (1). The presence of AGWs modifies the atmosphere and ionosphere which in turn alters the characteristics

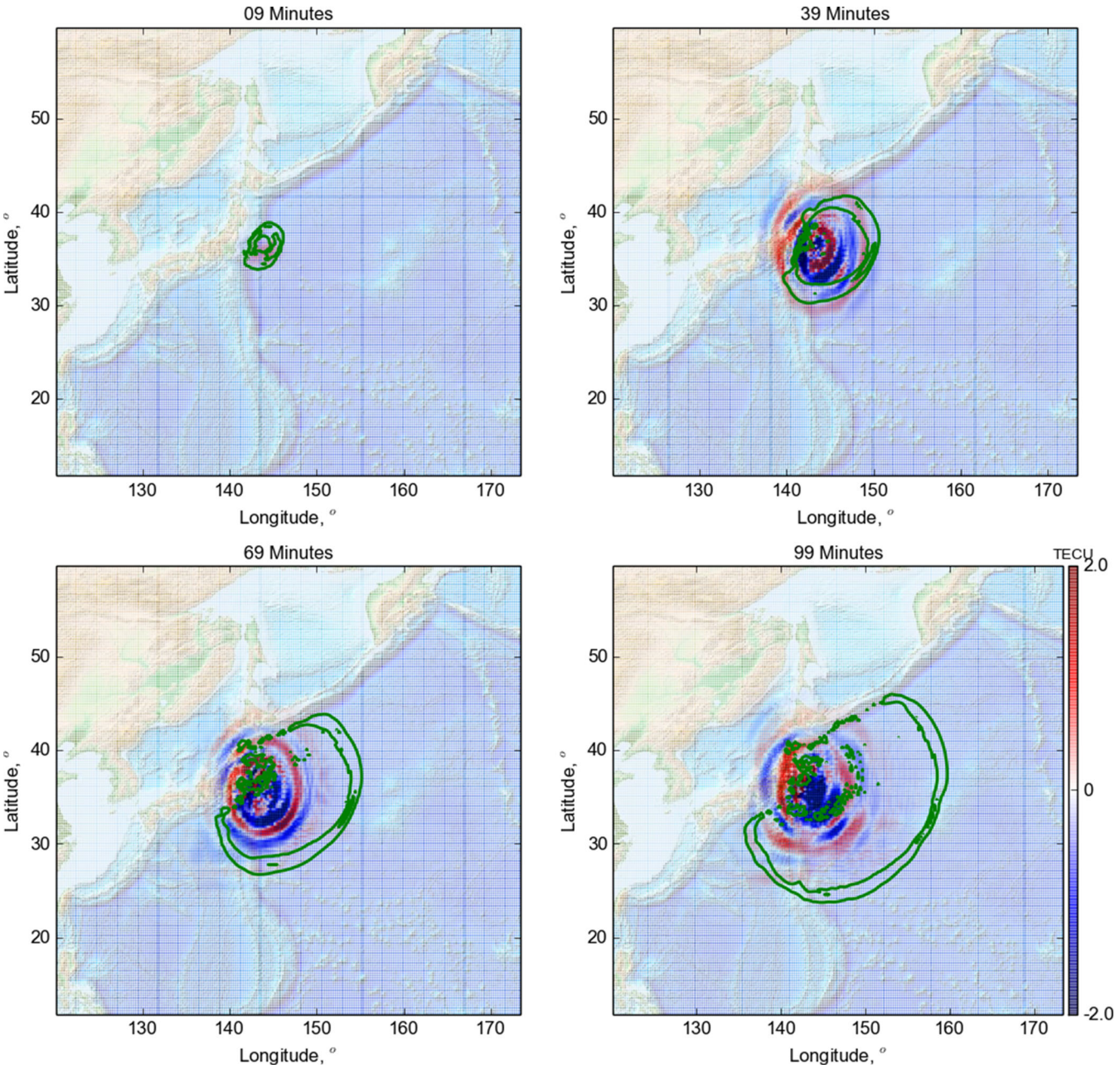

Figure 2. Snapshots of the simulation results for Case I at few selected times. The background image represents the spatial distribution of ΔTEC disturbance with on top the green contours corresponding to the principal wave front of the tsunami. The ΔTEC disturbance is defined as the integrated $\Delta n = n(t) - n_o$ between 200 and 300 km altitudes where $n(t)$ and n_o are the number densities of electrons at current and initial times.

of AGWs itself. This cause-effect mechanism continues for next 3 hr which is the time chosen to stop the simulation.

3 RESULTS

We examine the following two cases: excitation of primary AGWs/secondary dominant GWs (Case I) and excitation of primary/secondary AGWs or complete AGWs (Case II). The primary and secondary waves are oblique propagating waves having their propagation wave vectors more aligned in radial and horizontal directions, respectively (Kherani *et al.* 2012).

Under Case I, the excitation of dominant GWs is accomplished by ignoring the viscous dissipation terms in the horizontal components of the wave eq. (1) while retaining them in the radial component, that is, only this component participates in the generation of secondary AGWs. This condition favours the excitation of secondary radial wind component from the radial thrust of dissipated primary radial component. In turn, this secondary component acts like a transverse component for the dominantly horizontal propagating secondary AGWs, that is, the secondary waves become dominantly GWs. Under Case II, the viscous terms in both horizontal and radial components of the wave eq. (1) are retained, which is a realistic scenario that excites the complete AGWs.

In Figs 2 and 3, respectively, results corresponding to Cases I and II are shown wherein, colour images or pixmaps represent the horizontal distribution of TEC disturbance (ΔTEC), at few selected times (as mentioned at the top of each panel). Here, ΔTEC is the

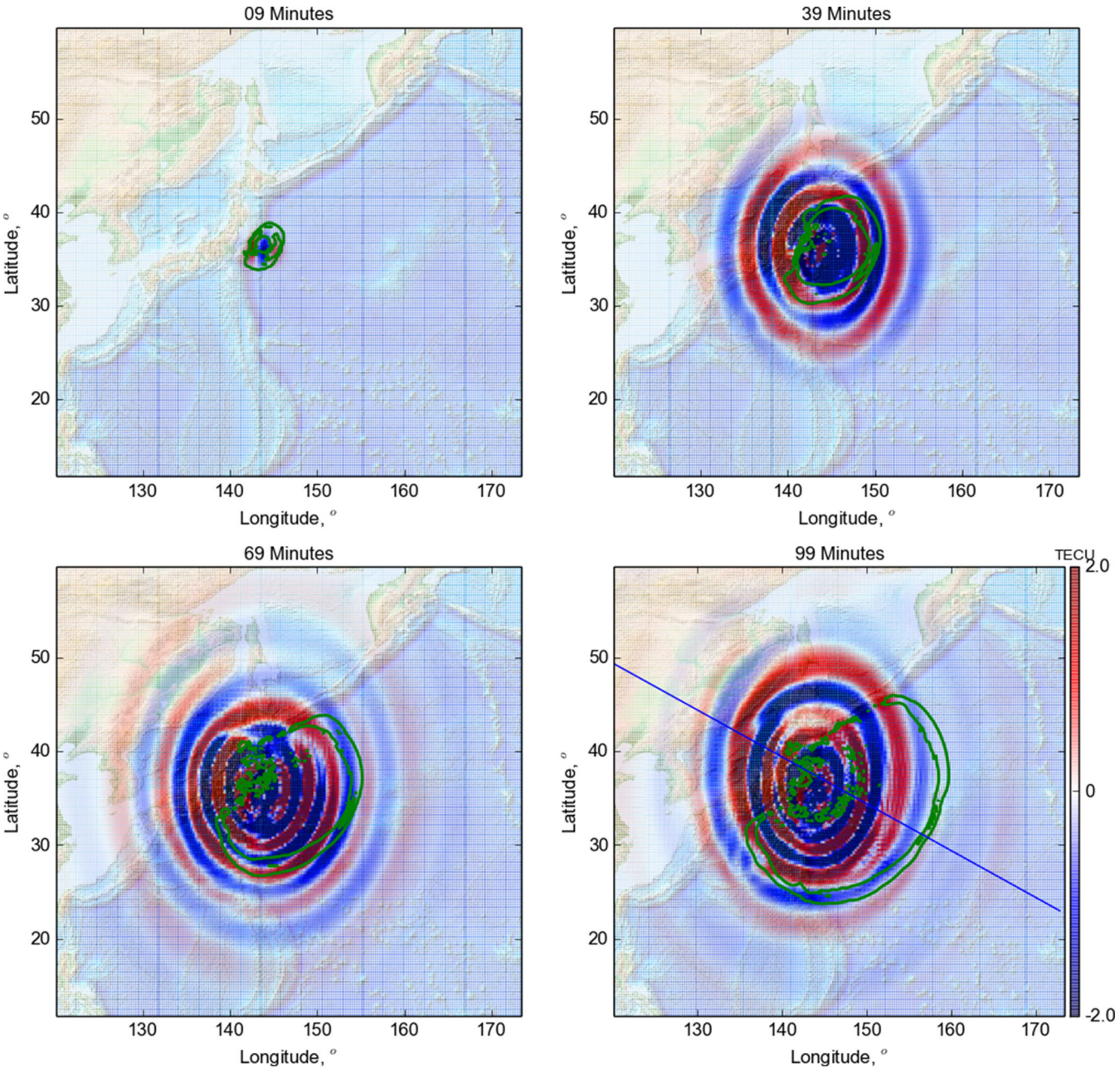

Figure 3. Simulation results for Case II in same format as Fig. 2.

integrated $\Delta n = n(t) - n_o$ between 200 and 300 km altitudes where $n(t)$ and n_o are the number densities of electrons at current and initial times. In these plots, also superimposed are the instantaneous principal tsunami wave fronts, represented by the green contours.

From Fig. 2, we note the following characteristics: (A) ΔTEC $\sim$ 2TECU are excited, (B) they remain behind by $\sim 1^\circ$–3° from the principal tsunami wave fronts at any given time, (C) absence of ΔTEC disturbances ahead of the tsunami wave fronts.

From Fig. 3, we note the following characteristics: (D) ΔTEC $\sim$ 2TECU are excited behind and in the vicinity of the principal tsunami wave front, (E) during 39–99 min when the tsunami travels through $\sim 6^\circ$–12° of epicentral distance, ΔTEC $\sim$ 1TECU are present ahead of the tsunami wave front covering $\sim 3^\circ$–10° from the tsunami location, (F) they have comparatively longer wavelength than those excited behind the tsunami wave front.

4 DISCUSSION

4.1 Strong forcing from the secondary AGWs in comparison to the secondary GWs

The tsunami wavefield, shown in Figs 2 and 3 as green contours, excites the primary AGWs that in turn, excite the secondary AGWs. In addition to the horizontally propagating tsunami wavefield, these obliquely propagating secondary AGWs are responsible for the horizontal spreading of the ΔTEC disturbances or TIDs. These aspects are discussed in our previous work (Kherani *et al.* 2012) in the context of CTIDs. In this study, we focus on the TIDs which are propagating ahead of the tsunami wave front as noted under (E–F). These anomalies are referred as Ahead-of-Tsunami-TIDs or ATIDs.

The characteristics noted under (A–F) suggest that in spite the identical tsunami propagation under Cases I and II, the horizontal distributions of TIDs are drastically different. A noteworthy difference is that under Case I, only CTIDs are excited while under Case II, both CTIDs and ATIDs are excited. This difference indicates the diverse effects of the nature of secondary wave on the generation of different kinds of TIDs. Under Case I, only the dissipation of radial momentum of the dominantly radial propagating primary AGWs is included. Therefore CTIDs are arising from the dissipation of longitudinal mode. On the other hand, ATIDs are arising from the dissipation of the horizontal momentum which is included under Case II. Moreover, since the horizontal momentum are associated with the transverse mode of the dominantly radial propagating primary AGWs, it can be said that the dissipated GW mode is responsible for the generation of ATIDs. We also note from Fig. 3 that the wavelengths of CTIDs and ATIDs are $\sim 3^\circ$ and $\sim 6^\circ$, respectively, that is, they are short and long wavelength TIDs, respectively.

These ATIDs propagate horizontally, much faster than the tsunami itself and reach farther distances, at any given time. We note from Fig. 3 that during 39–99 min when the tsunami travels through $\sim 6^\circ$–12° of epicentral distance, strong ATIDs propagate ahead of tsunami, covering $\sim 3^\circ$–10° of distance from the tsunami wave front. This means that, considering tsunami velocity ~ 250 m s^{-1}, these ATIDs arrive $\sim$20–60 min earlier (than the tsunami itself) at locations which are 3°–10° ahead of the instantaneous tsunami arrival locations. This is a novel outcome of this study that classifies ATID as a potential candidate for the early warning of tsunami yet their systematic presence needs to be confirmed from observations and other events. In Section 4.3, we present a set of observations from which we confirm the presence of ATIDs. At this point, we cite the first observation of tsunamigenic-TIDs from an all-sky imager over a far-field station, Hawaii (Makela *et al.* 2011) that revealed the presence of TIDs behind and ahead (or early) of the tsunami wave front. In addition to the various possible mechanisms discussed by Makela *et al.* (2011), the generation mechanism of ATIDs discussed in this study offers another plausible interpretation for the observed early waves over Hawaii.

In Fig. 3, TIDs are elongated in the north–south direction suggesting that they are propagating faster in this direction as compared to east–west. This preferred direction is partly due to the tsunami waveform which is more elongated in north–south and partly due to large mobilities of ions and electron along the geomagnetic field lines in the F region. Also, owing to these large mobilities, the wave fronts of TIDs are thicker in the north–south than in the east–west direction.

We also note that the amplitude of TIDs varies with the epicentral distance. Strong TIDs reside near the epicentre and near the tsunami arrival location while in between them, relatively weaker TIDs are excited. Moreover, ahead of the tsunami arrival location, weaker TIDs are excited.

4.2 Propagation characteristics of the TIDs

In order to understand the dynamics of ATIDs in detail, we present traveltime diagram (TTD) in Fig. 4 for the realistic Case II. This TTD is constructed from the time evolution of TID along a chosen horizontal trajectory which is shown as blue line in Fig. 3. The colour image represents the TIDs and the green contours represent the maximum value of the principal tsunami wave front. We note that the tsunami wave front constructs a cone at the origin. The TIDs residing inside and outside this cone are identified as CTIDs and ATIDs, respectively. The positive and negative epicentre distances in Fig. 4 represent the forward or southeast and backward or northwest directions with respect to the tsunami propagation direction. For the Tohoku-Oki tsunami, observed TTDs are reported from both southeast and northwest directions (Rolland *et al.* 2011; Galvan *et al.* 2012).

In Fig. 4, we note the presence of varieties of wave fronts with slopes steeper, similar and shallower than the slope of the green (tsunami) wave front suggesting that these wave fronts propagate faster, similar and slower than the tsunami, respectively. More specifically, we note the following features: (G) the CTIDs and ATIDs are slower/similar and faster propagating wave fronts, respectively, (H) for the tsunami arrival at epicentre distance larger than $\sim 6^\circ$, ATIDs spread ahead upto 3°–10° from the arrival location, (I) amplitude of ATIDs decreases sharply with increasing epicentre distance, (J) similar kinds of CTIDs and ATIDs are excited in the southeast and northwest directions.

The simulated TTDs in Fig. 4 are similar to the observed TTDs (Liu *et al.* 2011; Rolland *et al.* 2011; Galvan *et al.* 2012; Occhipinti *et al.* 2013). A noteworthy similarity is the presence of tsunamigenic-TIDs traveling up to approximately ~ 2200 km $\approx 20^\circ$ epicentre distance in the west/northwest direction. Since tsunami propagation was restricted to $\sim 2^\circ$–3° of epicentral distance in the northwest direction, presence of TIDs in this direction similar to the southeastward TIDs is intriguing. We attempt to explain it as follows: In Fig. 4, we note that the tsunami traveled in both directions during first $\sim$40 min and acquires large amplitude towards northwest due to the decreasing water depth. It also acquires large impulsive amplitude as it strikes the coast near $\sim 2^\circ$–3° of epicentral distance. This amplification favours strong forcing and subsequent generation of AGWs towards northwest as also suggested by Galvan *et al.* (2012). These forcing factors together with the efficient coupling of AGWs with the ionosphere along the geomagnetic field lines favour the strong and fast propagating northwestward TIDs similar to the southeastward TIDs.

In Fig. 4, we also note the presence of slow propagating northwest TIDs after 40 min. They arise from the forcing of the tsunami waves trapped along the coast which last for longer times as noted in Fig. 4.

From Fig. 4, we note that ATIDs (and also the far-field CTIDs residing at epicentral distance larger than 6°) are relatively longer period ($>$15 min) disturbances in comparison to the near-field CTIDs residing within 6° of epicentral distance which have periods between $\sim$5 and 10 min. Yet, the longer period ATIDs propagate much faster than the shorter period near-field CTIDs. In Section 4.1, we noted that the ATIDs and CTIDs are associated with the dissipation of transverse and longitudinal modes of the primary AGWs, respectively. These dissipated modes become longitudinal and transverse forcing for the secondary AGWs, respectively and as a result, ATIDs and CTIDs acquire longer and shorter wavelengths (as noted from Fig. 3). This evolution in the wavelength content alone can explain why ATIDs propagate faster than CTIDs, and rapidly appear ahead of the tsunami wave front.

In general, the acoustic and GW features noted in Fig. 4 are arising from the dissipation of the AGWs triggered by both earthquake and tsunami. The role of seismic triggered acoustic waves in the generation of CTIDs has been documented and simulated in the case of many past earthquakes (Calais & Minster 1995; Artru *et al.* 2005; Heki & Ping 2005; Kherani *et al.* 2009; Lognonné 2009) while the role of tsunami triggered GWs to generate the CTIDs is

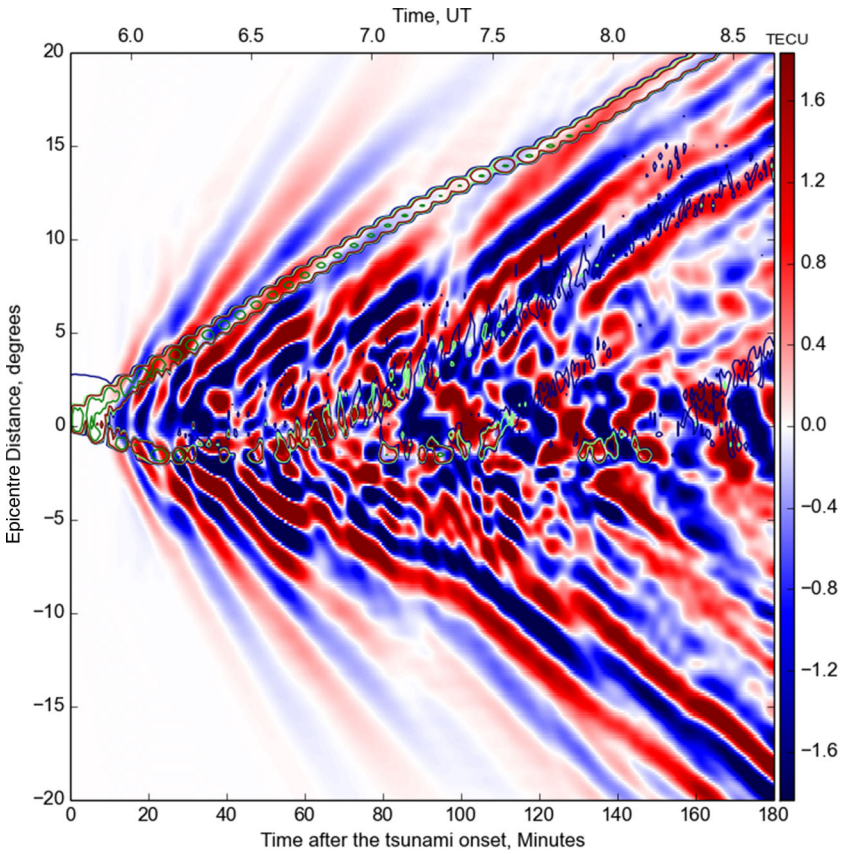

Figure 4. Simulated traveltime diagram (TTD) for the realistic Case II. This TTD is constructed by time scanning the ΔTEC along a chosen horizontal trajectory which is shown as a blue line in Fig. 3. The background image represents the ΔTEC disturbance or TIDs and the green-blue contours represent contours of the main, simulated, tsunami waves.

restricted to fewer and more recent events and studies (Occhipinti *et al.* 2006, 2011, 2013; Rolland *et al.* 2010). This study captures the effects of both earthquake and tsunami owing to the inclusion of the dynamics of both acoustic and GWs.

4.3 Interpreting the observations

Figs 5(a) and (b) depict, respectively, the ΔTEC disturbances measured by receiver 1098 along the trajectory of satellite PRN 12 and by receiver CNMR along the trajectory of satellite PRN27. Based on the low-pass filtered data and corresponding wavelet spectra shown in lower two panels, we note the presence of two amplified wave phases in ΔTEC: an N-shaped largest or primary maximum appearing 10–20 min after the tsunami arrival and a second largest or secondary maximum appearing 90–30 min prior to the tsunami arrival. We identify the primary maximum of ΔTEC as the signature of CTIDs. This result is supported by studies of the Tohoku-Oki tsunami and other events (Rolland *et al.* 2010, 2011) which detected CTIDs 10–45 min after the tsunami arrival. On the other hand, the presence of secondary maxima prior to the tsunami arrival was not examined in the previous studies. The possibility that such maxima are of the tsunamigenic nature, can be confirmed if complemented with the simulation results.

In panels (a) and (b) of Fig. 6, respectively, the simulated ΔTEC at receiver location 1098 along the trajectory of PRN12 and at receiver location CNMR along the trajectory of PRN27 are shown. We note that the low-pass filtered simulated ΔTEC have similar waveforms and wavelet spectra as noted in the measurements, revealing the presence of N-shaped primary maxima and secondary maxima that appear after and before the tsunami arrival, respectively. The simulated secondary maxima correspond to ATIDs in Figs 3 and 4 and therefore the observed secondary maxima in Fig. 5 are of tsunamigenic nature and can be classified as ATIDs.

If the observed ΔTEC from Fig. 5 are not interpreted by the simulation results, then the observed secondary maxima, that appear prior to the tsunami arrival, may be identified as precursors, leading to a wrong interpretation. However, as the simulation results suggest, these observed secondary maxima are propagating ahead of the tsunami, generated by the tsunami itself and therefore, they are not the tsunami precursors.

While we find a good agreement between the amplitude of the observed and simulated ΔTEC for CTIDs, our simulation does not reproduce well the amplitude of ATIDs. Since CTIDs are excited by the primary tsunami forcing, we expect a good agreement since the simulated tsunami reproduces the naturally occurred tsunami very well. On the contrary, ATIDs are excited by the secondary forcing developed in the thermosphere, therefore they are more sensitive to the ambient thermospheric conditions, namely, to the horizontal distribution of density, temperature and mean winds. These atmospheric variables are derived from the empirical models and may differ from the real thermospheric conditions prevailing during the event. These differences can lead to the difference in the amplitudes of simulated ATIDs and measured ATIDs.

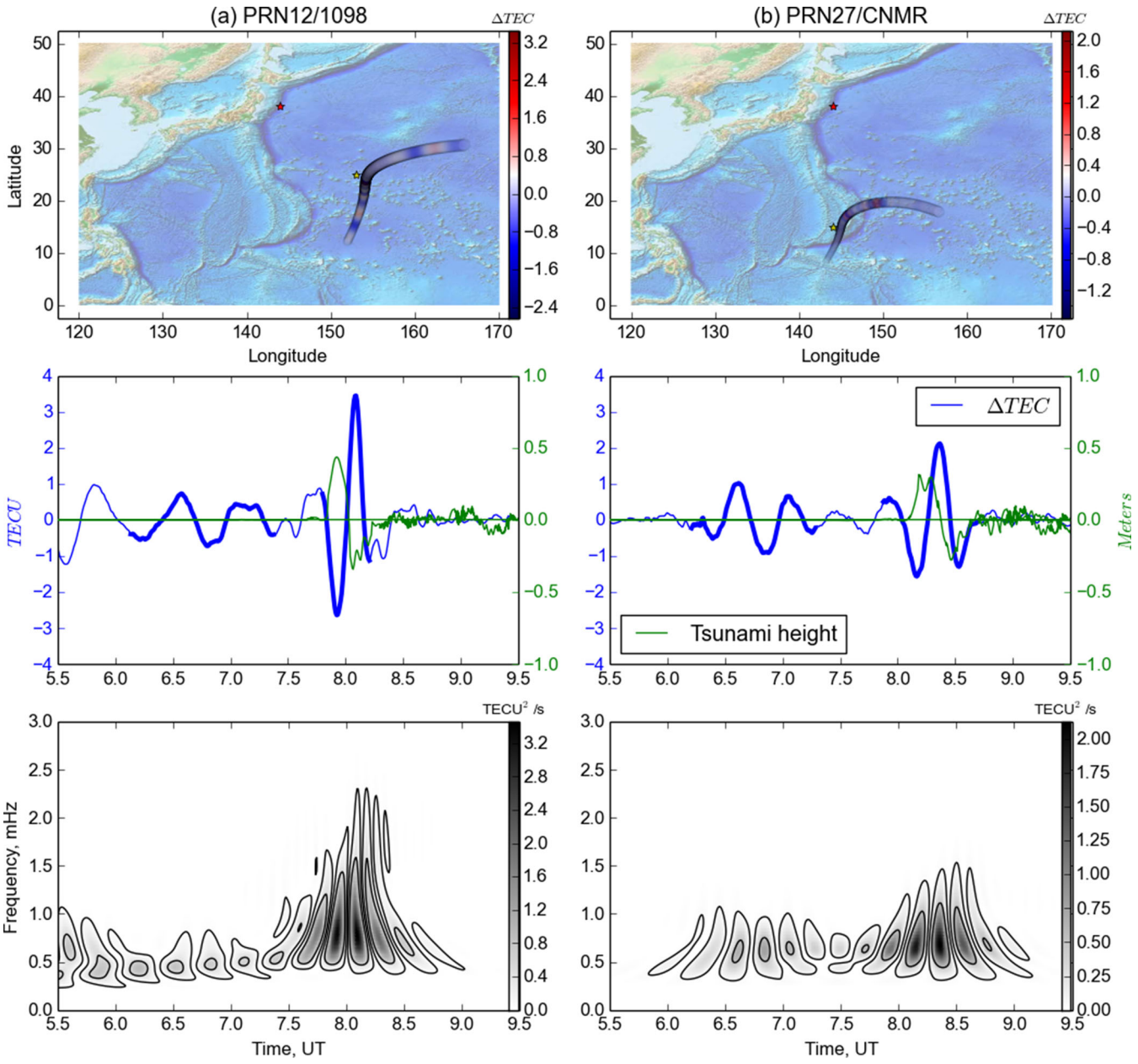

Figure 5. In panels (a) and (b), the observed ΔTEC or TIDs measured from PRN12/1098 and PRN27/CNMR are shown, respectively. Here, PRN12 and PRN27 are the GPS satellites and 1098 and CNMR are the receiver locations. In the upper panels, red and yellow stars represent the locations of the epicentre and receiver locations, respectively and colour images represent the ΔTEC along the trajectories of satellites. In the middle panels, blue curves represent the low-pass filtered (less than 5 mHz) ΔTEC and green curves represent the simulated tsunami wavefield. The lower plots are the wavelet spectra of the above ΔTEC time-series.

We note that both CTIDs and ATIDs cover the spectral range between 0.5 and 1 mHz (or 32–16 min) with a spectral peak around 0.5 mHz. However, CTIDs are horizontally short waves (with wavelength ∼3°) and ATIDs are horizontally long waves (with wavelength ∼6°) (as noted in Fig. 3). Hence despite similar frequencies, ATIDs propagate faster than CTIDs (as noted in Fig. 4) because of their longer wavelength.

The simulated ΔTEC in Fig. 6 corresponds to the integrated Δn between 200 and 300 km altitude. In order to study the behaviour of ΔTEC with varying altitude range of integration, we present the simulated ΔTEC corresponding to the integration of Δn between 200 and 400 km altitude in Fig. 7. We note that while the disturbances are similar in the low-frequency domain (less than 1 mHz), the simulated ΔTEC from higher altitude integration creates additional high-frequency perturbations. This high-frequency contribution is from the new waves generated above 300 km altitudes due to artefact of the simulation in extremely rarefied atmosphere at these altitudes while the simulation still preserves the low-frequency contribution due to AGWs. Therefore, the largest contribution to ΔTEC is indeed from the 200 and 300 km altitude range and the attenuation effects including the attenuation of high-frequency artefacts above 300 km should be larger than currently modeled.

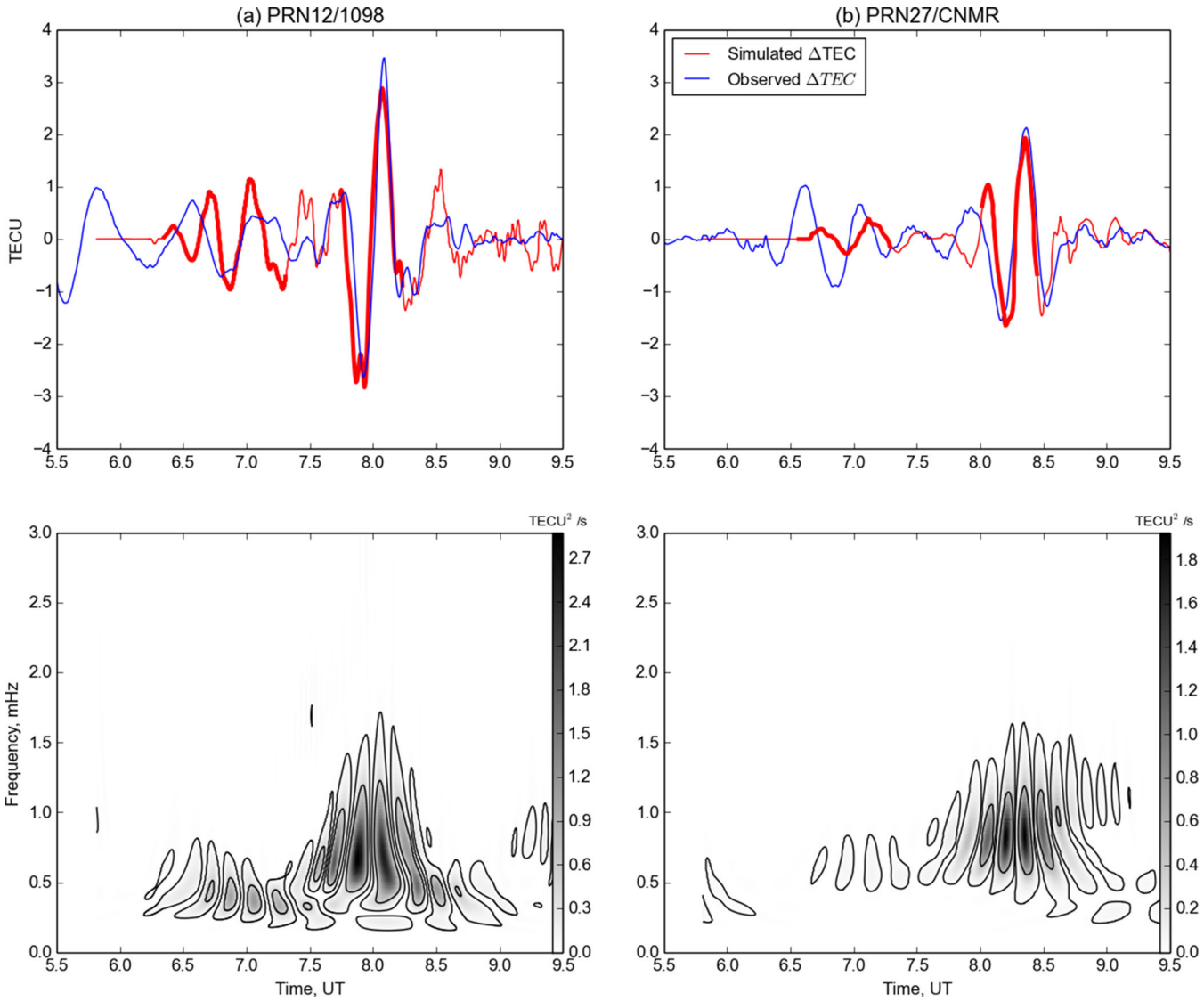

Figure 6. In panels (a) and (b), the simulated ΔTEC from PRN12/1098 and PRN27/CNMR are shown, respectively. In the upper panels, red and blue curves represent the low-pass filtered (less than 5 mHz) ΔTEC from simulation and observation respectively. The lower plots are the wavelet spectra of the above ΔTEC time-series. Here, ΔTEC is obtained by integrating Δn between 200 and 300 km altitude ranges.

5 CONCLUSIONS

In this study, we report on the simulation and observations of two kinds of TIDs associated to the Tohoku-Oki tsunami. These TIDs are referred as CTIDs and ATIDs which are excited behind and ahead of the principal tsunami wave front, respectively.

Two comparative scenarios, representing the excitations of dominant secondary GWs and of complete secondary AGWs, are examined to understand the origin of ATIDs. We find that the dominant secondary GW scenario only excites CTIDs of ∼2 TECU while the complete AGWs scenario is also able to excite ATIDs of ∼1 TECU. This second scenario reveals that the tsunamigenic-TIDs cover a wider area in the ionosphere than the tsunami itself. When the tsunami propagates between ∼6° and 12° of epicentral distance, ATIDs arrive ∼20–60 min earlier, covering 3°–10° of distance ahead of the tsunami. The study demonstrates ability of the secondary AGWs to gives rise to highly energetic rapidly developing ATIDs. These ATIDs are generated from the horizontal thrust arising from the dissipation of horizontal momentum of AGWs in the thermosphere and consequently they are associated to the GW modes and acquire long horizontal wavelengths owing to the horizontal thrust.

Observations of TIDs along the trajectories of two GNSS satellites are presented and compared to our simulated TIDs. Observed features such as the presence of two clear wave phases representing primary and secondary maxima, their time of occurrence, waveform and spectral characteristics are reproduced reasonably well in the simulation though the secondary maxima differ in amplitude. In both the observations and the simulation, ATIDs are identified as the secondary maxima in the temporal variation of TIDs that appear 30–90 min prior to the tsunami arrival.

The early presence (as early as 60 min prior to the tsunami arrival) of TIDs in the ionosphere at 10° ahead of the tsunami wave front makes them as an important observable for the detection of tsunami in the far field. Because it relies on the existing and continuously growing GNSS networks, it could complement the existing tsunami early warning systems at an effective cost.

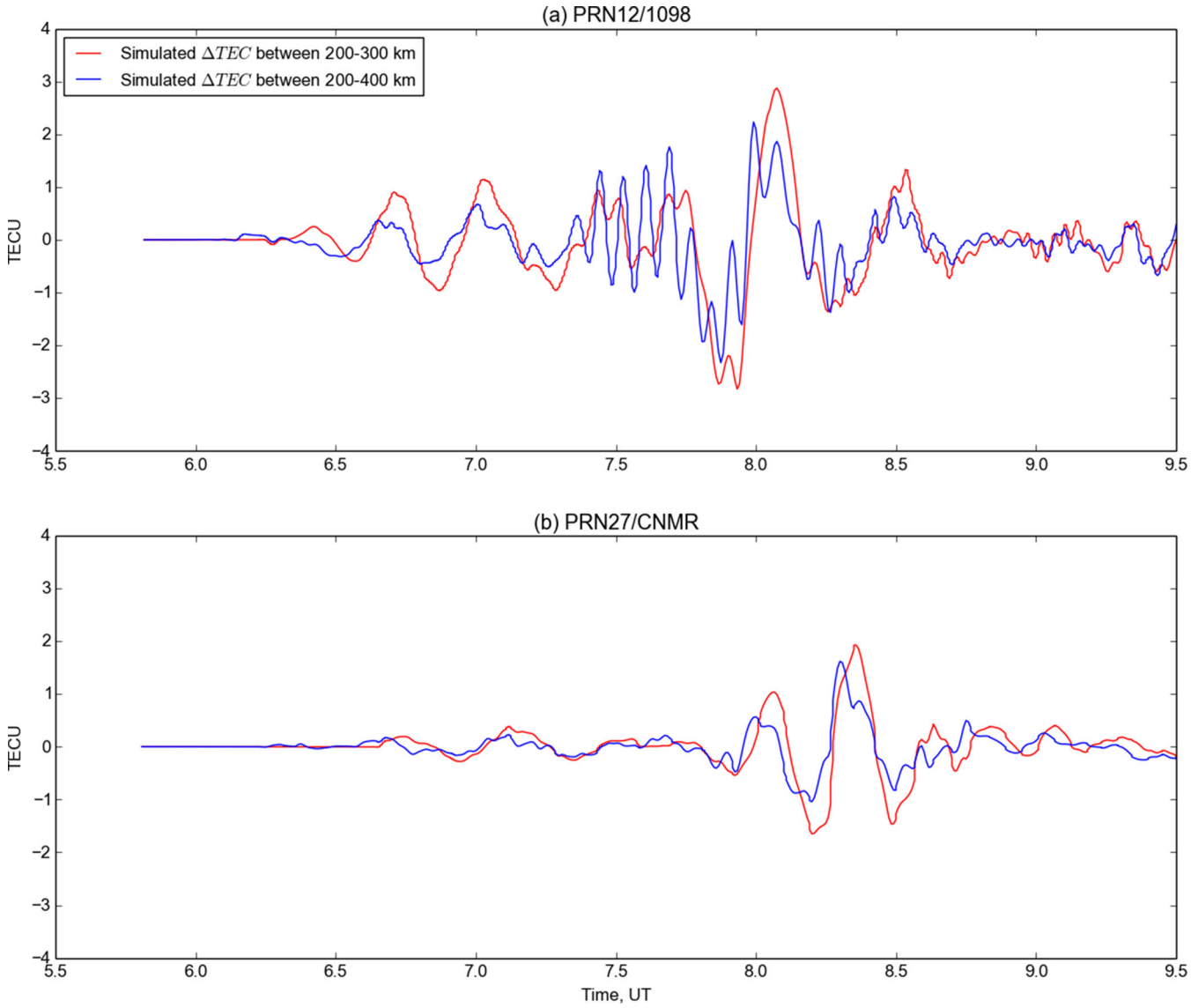

Figure 7. In the upper and lower panels, the simulated ΔTEC from PRN12/1098 and PRN27/CNMR are shown, respectively. The blue curves correspond to the ΔTEC obtained by integrating Δn between 200 and 400 km altitude ranges. The red curves from the upper panels of Fig. 6 are replotted for comparison.

ACKNOWLEDGEMENTS

This work is carried out with the funding from FAPESP-Brazil under process (2011/21903-3) and ANR-France under project TO_EOS (ANR-11-JAPN-008).

REFERENCES

Artru, J., Ducic, V., Kanamori, H., Lognonné, P. & Murakami, M., 2005. Ionospheric detection of gravity waves induced by tsunamis, *Geophys. J. Int.,* **160,** 840–848.

Astafyeva, E., Lognonné, P. & Rolland, L., 2011. First ionosphere images for the seismic slip of the Tohoku-oki earthquake, *Geophys. Res. Lett.,* **38,** L22104, doi:10.1029/2011GL049623.

Astafyeva, E., Rolland, L., Lognonné, P., Khelfi, K. & Yahagi, T., 2013. Parameters of seismic source as deduced from 1 Hz ionospheric GPS data: case study of the 2011 Tohoku-oki event, *J. geophys. Res.,* **118**(9), 5942–5950.

Bletery, Q., Sladen, A., Delouis, B., Valle, M., Nocquet, J.-M., Rolland, L. & Jiang, J., 2014. A detailed source model for the Mw9.0 Tohoku-Oki earthquake reconciling geodesy, seismology, and tsunami records, *J. geophys. Res.,* **119,** 7636–7653.

Calais, E. & Minster, J.B., 1995. GPS detection of ionospheric perturbations following the January 17, 1994, Northridge earthquake, *Geophys. Res. Lett.,* **22,** 1045–1048.

Chen, C.H. *et al.*, 2011. Long-distance propagation of ionospheric disturbance generated by the 2011 off the Pacific coast of Tohoku Earthquake, *Earth Planets Space,* **63,** 881–884.

Galvan, D.A., Komjathy, A., Hickey, M.P., Stephens, P., Snively, J., Tony Song, Y., Butala, M.D. & Mannucci, A.J., 2012. Ionospheric signatures of Tohoku-Oki tsunami of March 11, 2011: model comparisons near the epicenter, *Radio Sci.,* **47,** RS4003, doi:10.1029/2012RS005023.

Garcia, R.F., Doornbos, E., Bruinsma, S. & Hébert, H., 2014. Atmospheric gravity waves due to the Tohoku-Oki tsunami observed in the thermosphere by GOCE, *J. geophys. Res.,* **119**(8), 4498–4506.

Heki, K., 2011. Ionospheric electron enhancement preceding the 2011 Tohoku-Oki earthquake, *Geophys. Res. Lett.,* **38,** L17312, doi:10.1029/2011GL047908.

Heki, K. & Ping, J., 2005. Directivity and apparent velocity of the coseismic ionospheric disturbances observed with a dense GPS array, *Earth planet. Sci. Lett.,* **236,** 845–855.

Hébert, H., Heinrich, P., Schindel, F. & Piatanesi, A., 2001. Far-field simulation of tsunami propagation in the Pacific Ocean impact on the Marquesas Islands (French Polynesia), *J. geophys. Res.,* **106,** 9161–9177.

Huba, J., Joyce, G. & Fedder, J., 2000. Sami2 is Another Model of the Ionosphere (SAMI2): a new low latitude ionosphere model, *J. geophys. Res.,* **105**(A10), 23 035–23 053.

Kherani, E.A., Lognonné, P., Kamath, N., Crespon, F. & Garcia, R., 2009. Response of the ionosphere to the seismic triggered acoustic waves: electron density and electromagnetic fluctuations, *Geophys J. Int.,* **176,** 1–13.

Kherani, E.A., Abdu, M.A., Fritts, D. & de Paula, E.R., 2011. The acoustic gravity wave induced disturbances in the equatorial Ionosphere, in *Aeronomy of the Earth's Atmosphere and Ionosphere,* eds Abdu, M.A., Pancheva, D. & Bhattacharyya, A., Springer-IAGA Spacial Soporan Book Series, doi:10.1007/978-94-0326-1-10.

Kherani, E.A. *et al.*, 2012. Modelling of the total electronic content and magnetic field anomalies generated by the 2011 Tohoku-oki tsunami and associated acoustic-gravity waves, *Geophys. J. Int.,* **191**(3), 1049–1066.

Liu, J.Y., Chen, C.H. Lin C., Tsai, H.F., Chen, C.H. & Kamogawa, M., 2011. Ionospheric disturbances triggered by the 11 March 2011 M9.0 Tohoku earthquake, *J. geophys. Res.,* **116,** A06319, doi:10.1029/2011JA016761.

Lognonné, P., 2009. Seismic waves from atmospheric sources and Atmospheric/Ionospheric signatures of seismic waves, in *Infrasound Monitoring for Atmospheric Studies,* pp. 281–304, eds Le Pichon, A., Blanc, E. & Hauchecorne, A., Springer, Dordrecht, Netherlands.

Maeda, T., Furumura, T., Sakai, S. & Shinohara, M, 2011. Significant tsunami observed at ocean-bottom pressure gauges during the 2011 off the Pacific coast of Tohoku Earthquake, *Earth Planets Space,* **63,** 803–808.

Makela, J.J. *et al.*, 2011. Imaging and modeling the ionospheric airglow response over Hawaii to the tsunami generated by the Tohoku earthquake of 11 March 2011, *Geophys. Res. Lett.,* **38,** L00G02, doi:10.1029/2011GL047860.

Matsumura, M., Saito, A., Iyemori, T., Shinagawa, H., Tsugawa, T., Otsuka, Y., Nishioka, M. & Chen, C.H., 2011. Numerical simulations of atmospheric waves excited by the 2011 off the Pacific coast of Tohoku Earthquake, *Earth Planets Space,* **63,** 885–889.

Occhipinti, G., Lognonné, P., Kherani, E.A. & Hébert, H., 2006. Three-dimensional waveform modeling of ionospheric signature induced by the 2004 Sumatra tsunami, *Geophys. Res. Lett.,* **33,** L20104, doi:10.1029/2006GL026865.

Occhipinti, G., Coisson, P., Makela, J.J., Allgeyer, S., Kherani, E.A., Hébert, H. & Lognonné, P., 2011. Three-dimensional numerical modeling of tsunami-related internal gravity waves in the Hawaiian atmosphere, *Earth Planets Space,* **63**(7), 847–851.

Occhipinti, G., Rolland, L., Lognonné, P. & Watada, S., 2013. From Sumatra 2004 to Tohoku-Oki 2011: the systematic GPS detection of the ionospheric signature induced by tsunamigenic earthquakes, *J. geophys. Res.,* **118,** 3626–3636.

Rolland, L.M., Occhipinti, G., Lognonné, P. & Loevenbruck, A., 2010. Ionospheric gravity waves detected offshore Hawaii after tsunamis, *Geophys. Res. Lett.,* **37,** L17101, doi:10.1029/2010GL044479.

Rolland, L.M., Lognonné, P., Astafyeva, E., Kherani, E.A., Kobayashi, N., Mann, M. & Munekane, H., 2011. The resonant response of the ionosphere imaged after the 2011 Tohoku-Oki earthquake, *Earth Planets Space,* **63**(7), 853–857.

Simons, M. *et al.*, 2011. The 2011 Magnitude 9.0 Tohoku-Oki earthquake: megathrust from seconds to centuries, *Science,* **332**(6036), 1421–1425.

Sladen, A., Tavera, H., Simons, M., Avouac, J.P., Konca, A.O., Perfettini, H. & Cavagnoud, R., 2010. Source model of the 2007 Mw 8.0 Pisco, Peru earthquake: Implications for seismogenic behavior of subduction megathrusts, *J. geophys. Res.,* **115,** B02405, doi:10.1029/2009JB006429.

Tsugawa, T., Saito, A., Otsuka, Y., Nishioka, M., Maruyama, T., Kato, H., Nagatsuma, T. & Murata, K.T., 2011. Ionospheric disturbances detected by GPS total electron content observation after the 2011 Tohoku Earthquake, *Earth Planets Space,* **63**(7), 875–879.